Extreme Mechanics Letters 6 (2016) 37–44

Contents lists available at ScienceDirect

Extreme Mechanics Letters

journal homepage: www.elsevier.com/locate/eml

Debonding at the interface between active particles and PVDF binder in Li-ion batteries

Seungjun Lee [a,b], Jun Yang [c], Wei Lu [b,*]

[a] Department of Mechanical, Robotics and Energy Engineering, Dongguk University-Seoul, 100715 Seoul, Republic of Korea
[b] Department of Mechanical Engineering, University of Michigan, Ann Arbor, MI 48109, USA
[c] School of Chemistry and Chemical Engineering, Shanghai Jiao Tong University, Shanghai 200240, China

GRAPHICAL ABSTRACT

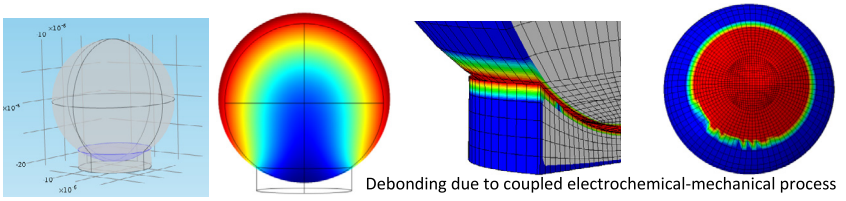

HIGHLIGHTS

- Studied debonding at the interface between particle and binder in a battery.
- Integrated electrochemical–mechanical model and cohesive zone model.
- Debonding is more likely to happen as the particle size and C-rate decrease.
- The trend of debonding is opposite to that of fracture inside a particle.
- Debonding is closely related to the total amount of lithium intercalation.

ARTICLE INFO

Article history:
Received 25 June 2015
Received in revised form 21 November 2015
Accepted 22 November 2015
Available online 2 December 2015

Keywords:
Battery
Electrochemical–mechanical model
Debonding

ABSTRACT

Mechanical failure in the electrode is one of major reasons for capacity fade. In this study we focus on inter-particle fracture, specifically the debonding at the interface between the graphite particle and binder. We integrate the electrochemical–mechanical model and the cohesive zone model to investigate the interfacial debonding during lithium intercalation. We found that the mechanism of fracture at the particle/binder interface is different from that inside a particle. The debonding at the interface is caused by the expansion of the particle that is closely related to the total amount of lithium intercalation, while the fracture inside a particle is caused by the gradient of lithium concentration. As a result, debonding at the interface is more likely to occur as the particle size and C-rate decrease, which is opposite to the trend of fracture inside a particle that is more likely to occur as the particle size and C-rate increase. This understanding of debonding mechanism can provide insight into capacity fade and guide the development of more robust electrodes.

* Corresponding author. Tel.: +1 734 647 7858; fax: +1 734 647 3170.
E-mail address: weilu@umich.edu (W. Lu).

http://dx.doi.org/10.1016/j.eml.2015.11.005
2352-4316/

1. Introduction

Fracture in the electrode is known as one of the major causes for degradation in Li-ion batteries [1–3]. The effects include loss of electric contact, isolation of active materials from the conductive matrix, and increased cell internal resistance. Fracture also increases the exposure of active materials to the electrolyte, accelerating side-reactions and capacity fade. The fracture behavior inside a single particle has been addressed by several works. Zhao et al. studied the effect of particle size and charging rate on fracturing in an electrode particle and predicted the critical fracture conditions by the energy release rate [4]. Woodford et al. constructed a map showing the safe parameter regimes against fracture, which depended on the C-rates, particle size and fracture toughness of the material [5]. Bhandakkar et al. calculated the critical electrode size to avoid crack nucleation in a cylindrical electrode particle [6]. Zhu et al. evaluated the effects of current density, particle size and particle aspect ratio on crack initiation using the extended finite element method [7]. These studies have revealed the critical conditions that determine whether a crack will grow or not. Furthermore, Grantab et al. investigated the progressive propagation of a crack during cycling in a graphite particle [8] or in a silicon nanowire [9].

However, inter-particle fracture in electrode materials has rarely been addressed in theoretical studies. In an electrode, particles are connected together by the binder. Two scenarios can possibly happen for inter-particle fracture depending on the locations: fracture in the middle of binder or at the particle/binder interface. Recently, atomistic simulations have shown that the cohesive strength at the interface is weaker than that inside the binder, suggesting that inter-particle fracture is more likely to happen at the particle/binder interface [10].

In this paper, we study the debonding behavior between a graphite particle and a PVDF (polyvinylidene fluoride) binder associated with the electrochemical–mechanical processes during the operation of a Li-ion battery. Graphite particles and PVDF are commonly used as the anode material and the binder in current commercial batteries. To capture fracture at the interface, we have developed an electrochemical–mechanical model that incorporates the cohesive zone approach. First, diffusion-induced stresses are calculated by the electrochemical–mechanical model. Then, the lithium concentration profile is exported to the cohesive zone model by thermal stress analogy. Since the cohesive zone model can describe crack initiation and its propagation, the simulation results can provide quantitative insight into the debonding process during lithium intercalation and capture the creation of new interfaces that are exposed to the electrolyte.

In the cohesive zone model, the traction–separation curve is an important input. We have implemented the parameterized traction–separation curve obtained from atomistic calculations as input data for the cohesive zone model. Our study shows that the fracture mechanism at the particle/binder interface is significantly different from that inside a particle: the interfacial fracture is more likely to happen at small particle sizes and low C-rates, a trend that is opposite to that inside a particle. This paper is structured as follows. First, the theoretical framework for the calculation of lithium diffusion and the simulation of debonding at the interface are described. Then, simulation results with the electrochemical–mechanical model and the cohesive zone approach are shown. Finally, the conclusion is given at the end.

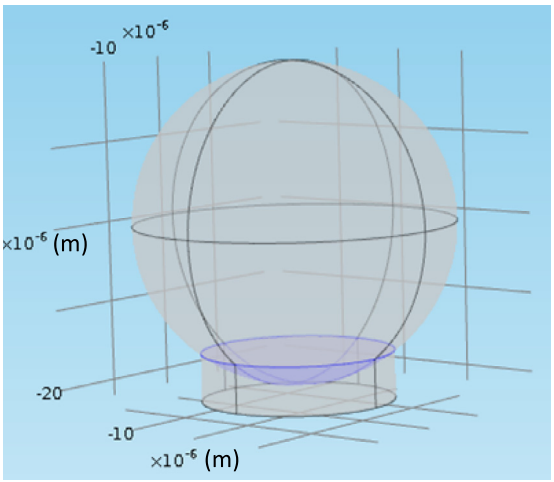

Fig. 1. The model system of a spherical graphite particle attached to a cylindrical PVDF binder.

2. Method

We consider a spherical graphite particle attached to a cylindrical PVDF binder, as shown in Fig. 1. A two-step method is used to study the interfacial debonding due to lithium intercalation. First, we calculate the diffusion-induced stress in the particle by coupling the stress field and Li-ion diffusion. Second, we export the calculated lithium concentration profile at a specific state of charge and apply it to the cohesive zone model to examine the debonding behavior.

2.1. Electrochemical–mechanical model

The stress–strain relation in the particle can be written as [11,12]

$$\varepsilon_{ij} = \frac{1}{E}\left[(1+\nu)\sigma_{ij} - \nu\sigma_{kk}\delta_{ij}\right] + \frac{c\Omega}{3}\delta_{ij}, \tag{1}$$

where ε_{ij} are strain components, E is Young's modulus, ν is Poisson's ratio, σ_{ij} are stress components, δ_{ij} is the Kronecker delta, c is the Li-ion concentration and Ω is partial molar volume of Li-ions. Comparing to the regular stress–strain relation, the last term in Eq. (1) is additional, which accounts for the strain due to Li-ion intercalation. In the binder region the regular stress–strain relation is applied. The mechanical boundary condition is given by constraining the displacements at the bottom of the binder, as shown in Fig. 1.

The gradient of chemical potential drives Li-ion diffusion. Both concentration and stress contribute to the chemical potential, leading to a diffusion flux of **J**,

$$\mathbf{J} = -D\left(\nabla c - \frac{\Omega c}{RT}\nabla\sigma_h\right), \tag{2}$$

where D is the diffusion coefficient of Li-ion, R is gas constant, T is absolute temperature, and σ_h is the hydrostatic stress given by $\sigma_h = (\sigma_{11} + \sigma_{22} + \sigma_{33})/3$. From the mass conservation, the time-dependent lithium concentration is given by

$$\frac{\partial c}{\partial t} + \nabla \cdot \mathbf{J} = 0. \tag{3}$$

Combining Eqs. (2) and (3) gives the diffusion equation with coupled concentration and stress field. The equation is solved with the initial condition of $c = 0$ in the particle and the boundary condition of

$$\mathbf{J} \cdot \mathbf{n} = \frac{i_n}{F}, \tag{4}$$

where $\mathbf{n}$ is the normal vector of the particle surface, i_n is the current density and F is Faraday's constant. The current density at the particle surface covered by the binder is set to zero. The current density at other regions on the particle surface is determined by the C-rate, which is

$$i_n = \text{C-rate}\frac{\alpha \rho R_s}{3}, \tag{5}$$

where α is the specific capacity of the particle, ρ is density and R_s is the radius of the particle.

The simulations are performed with the COMSOL Multiphysics software. The solid mechanics module (for stress calculation) and the PDE module (for diffusion calculation) are used simultaneously to solve the coupled mechanics and diffusion problem. In the solid mechanics module, the coupling is implemented by treating the lithium concentration c as 'temperature' and $\Omega/3$ in Eq. (1) as the 'coefficient of thermal expansion'. In the PDE module, the effect of stress field on diffusion, as shown in Eq. (2), is directly implemented.

2.2. Cohesive zone model

The cohesive zone model is developed using ABAQUS 6.11, which is equipped with cohesive elements that COMSOL lacks. The cohesive zone model allows overcoming the challenge of stress singularity in the classical continuum-based fracture analysis by incorporating the mechanism of fracture energy dissipation. The cohesive zone model has been widely used to model delamination and debonding of composites, metals, concrete, and polymers [13–17]. In the cohesive zone model, the fracture process is characterized by a traction–separation law across cohesive surfaces. In this study, we adapt a bilinear traction–separation law, where the governing parameters are the maximum stress and the fracture energy. The fracture process occurs on the cohesive surfaces as follows. The traction stress between two cohesive surfaces changes with the external loading. When the traction stress reaches the maximum stress, the delamination of surfaces or fracture initiates. Then the crack evolves until all of the fracture energy is dissipated and eventually, the fracture process is completed with the appearance of new surfaces, i.e. an advance of the crack. Crack growth is captured by tracking the crack advance step by step with the evolution of the external loading. In the cohesive zone model, the parameters of the traction–separation law are critical [18,19]. In this study, more accurate prediction is enabled by using the parameters obtained from atomistic simulations [10]. The main parameters such as the maximum stress, the maximum displacement and the displacement at the maximum stress are fitted into a bilinear traction–separation curve in the cohesive zone model.

Table 1
Damage criteria for the cohesive zone model.

	Normal	Shear
Initiation (maximum stress)	300 MPa	50 MPa
Evolution (fracture energy)	0.45 J/m^2	0.175 J/m^2
Initiation displacement	5 Å	20 Å

The lithium concentration profile from COMSOL output is loaded at the predefined 'temperature' field in ABAQUS. This thermal stress analogy reproduces the corresponding stress field. Cohesive elements are placed at the interface between the particle and the binder. The cohesive behavior is defined by two ingredients: "damage initiation" and "damage evolution". For the criteria of "damage initiation", the maximum nominal stress is prescribed in the normal and shear direction. For the criteria of "damage evolution", the fracture energy and a linear degradation model with uncoupled normal/shear modes are prescribed. Table 1 shows the values used in our calculations.

2.3. Material properties

Single crystal graphite has anisotropic material properties. However, the graphite particle for battery applications consists of multiple fine grains with random distributions, exhibiting macroscopic isotropic material properties. The volume change of a fully intercalated graphite anode particle is reported to be in the range of 8%–14%. We assume a 10% isotropic volume change [20] at the maximum Li intercalation concentration, $c_{\max}$, which corresponds to a volumetric strain of 0.0323. By thermal analogy in terms of volume expansion, $\Omega/3$ plays the same role as the thermal expansion coefficient [12]. The calculation gives

$$\Omega = \frac{3 \times 0.0323}{c_{\max}} = 3.6456 \times 10^{-6}\ \text{m}^3/\text{mol}. \tag{6}$$

The reported Young's modulus of PVDF ranges from 0.65 GPa to 8.3 GPa in the literature [21–25]. Here we take 2 GPa as its Young's modulus. The material properties used in calculations are summarized in Table 2.

3. Results

Fig. 2 shows the evolution of lithium concentration profile during charging (particle radius: 5 μm, 1 C-rate). In the early stage of evolution when lithium ions start to diffuse into the particle from the surface, the gradient of lithium concentration is fairly large, as shown in Fig. 2(a). After the interior of the particle is filled with more lithium ions, the gradient of lithium concentration becomes smaller, as shown in Fig. 2(b). For an isolated spherical particle in the electrolyte without any binder, the lithium concentration distribution is spherically isotropic with the lowest concentration at the particle center. In contrast, for the system

Table 2
Material properties used in the calculations.

Property	Units	Value
Diffusion coefficient of lithium (D) [25]	m^2/s	3.9×10^{-14}
Gas constant (R)	J/mol K	8.314
Temperature (T)	K	300
Partial molar volume of lithium (Ω)	m^3/mol	3.6456×10^{-6}
Maximum lithium concentration (c_{max}) [25]	mol/m^3	26 580
Graphite Young's modulus [26]	GPa	15
Graphite Poisson's ratio [26]		0.3
Graphite density	g/cm^3	2.2
PVDF Young's modulus	GPa	2
PVDF Poisson's ratio		0.32
PVDF density	g/cm^3	1.78

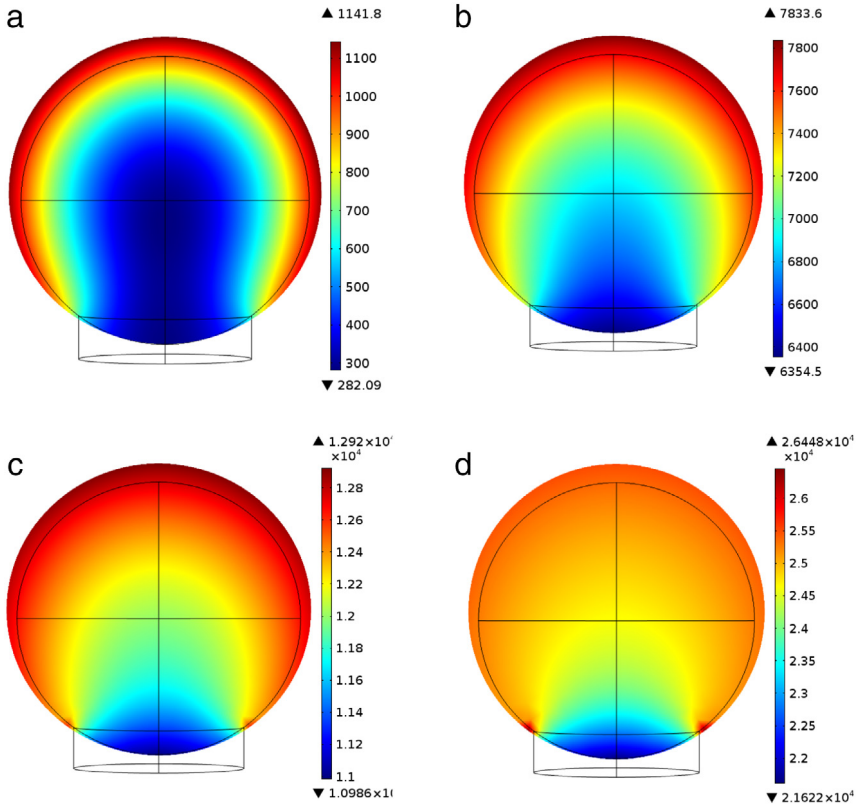

Fig. 2. The cross-section view of lithium concentration in the particle (particle radius: 5 μm, 1 C-rate) at time of (a) 100 s, (b) 1000 s, (c) 1700 s, (d) 3425 s.

studied here the lithium flux from the surrounding electrolyte is blocked by the binder at the particle/binder interface. The location of the lowest concentration appears at the bottom of the particle, rather than at the center of the particle, as shown in Fig. 2(b). After $t = 1400$ s, a zone with high lithium concentration begins to appear near the edge of the binder due to stress concentration. Fig. 2(c) shows such an example. The stress concentration is developed due to geometric discontinuity at the edge, which drives local lithium accumulation. At the late stage, the distribution of the lithium concentration becomes more uniform, as shown in Fig. 2(d), leading to an overall smaller concentration gradient inside the particle.

Fig. 3 shows the evolution of the maximum principal stress at the particle/binder interface. The blue line is calculated at the bottom of the particle while the red line is calculated at the edge of the particle/binder interface. The stress increases almost linearly as a function of time. The linear increase is caused by a gradual expansion of the particle, which is constrained by the binder below it. Therefore, the stress at the interface is mainly caused by the deformation of the particle due to lithium intercalation.

The debonding simulations are carried out for various states of charge (SOC). Representative results are shown in Fig. 4. For easy visualization, the view is from the bottom of the particle and the binder is removed to expose the debonded area. The red color region represents the locations where the particle is separated from the binder. Since the stress at the interface increases almost linearly, fracture at the interface is more likely observed at the

later stage during charging. In our simulations, debonding begins to occur at 85% SOC, showing a small portion of debonding near the edge of the binder. As SOC increases further, the debonding area is gradually enlarged toward the center. When the SOC reaches 95%, the binder is separated entirely. A clear view of separation is shown with a 3D section view at 100% SOC in Fig. 4(f). In Fig. 4, the circular asymmetry is due to using the hexahedral mesh, which results in directional mesh at the center of the bottom.

The simulation shows that the separation of the binder starts from the edge, which indicates that lithium ions can diffuse in through the crack at the interface. In the simulations we did not consider the change in the flux condition due to the creation of new surfaces, but will incorporate it in future studies.

We have investigated the effect of C-rate and particle size on the debonding behavior. Fig. 5 shows the debonding area for the fully charged state at different C-rates and particle sizes. For the particle radius of 5 μm, an entire separation occurs at 1 C-rate. However, at 5 C-rate only a small portion of separation is observed near the edge of the binder. When the particle size increases from 5 μm

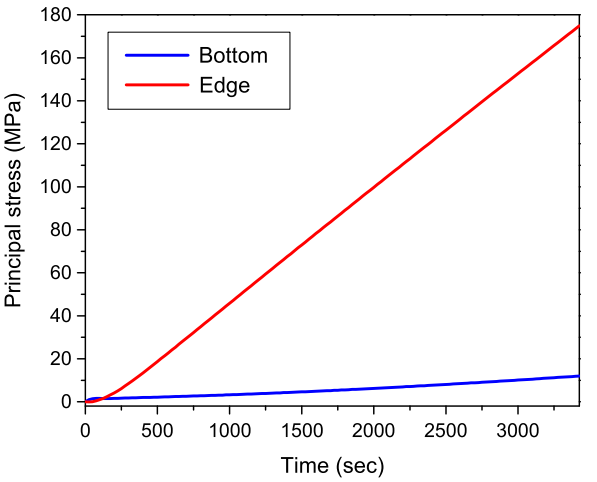

Fig. 3. Evolution of the maximum principal stress (Blue: at bottom of the particle, red: at the edge of the particle/binder interface). (For interpretation of the references to color in this figure legend, the reader is referred to the web version of this article.)

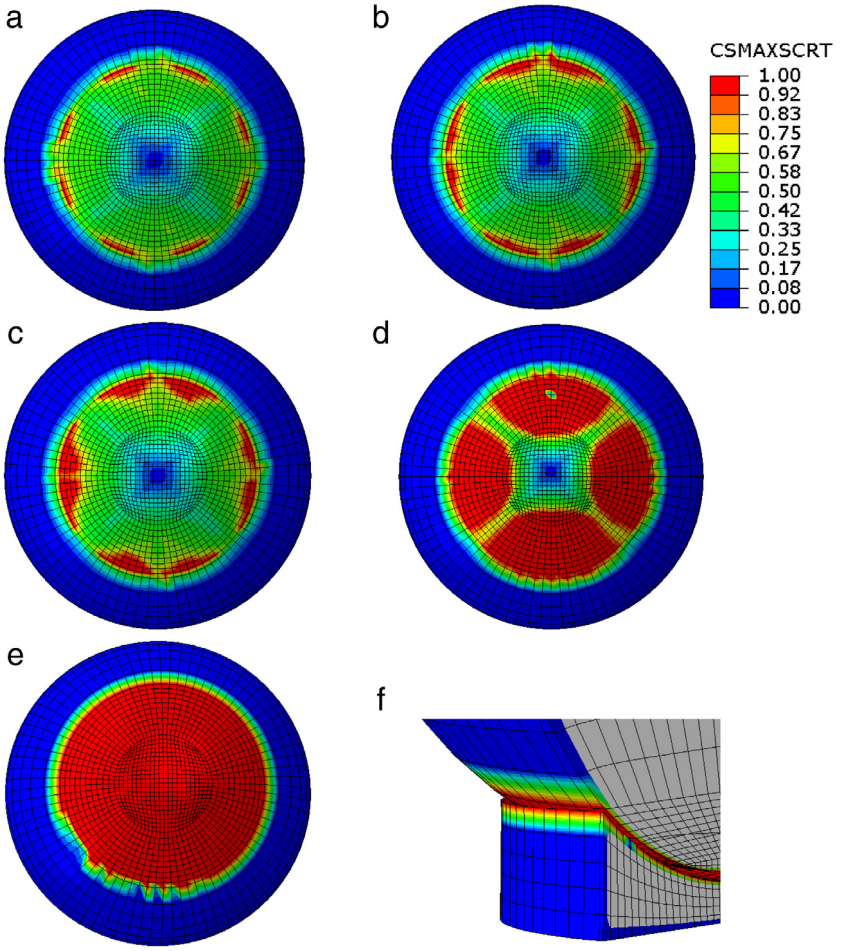

Fig. 4. Debonding areas at different SOCs. For easy visualization, the view is from the bottom of the particle and the binder is removed to expose the debonded area. The red color region represents the locations where the particle is separated from the binder. (a) 85% SOC, (b) 89% SOC, (c) 91% SOC, (d) 93% SOC, (e) 95% SOC, (f) 100% SOC (3D section view). (For interpretation of the references to color in this figure legend, the reader is referred to the web version of this article.)

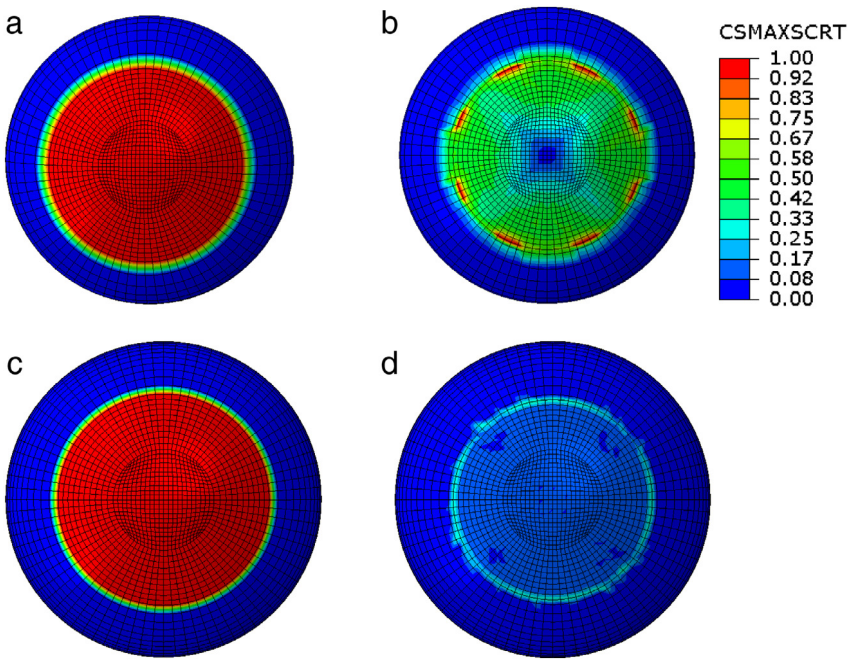

Fig. 5. Debonding areas at 100% SOC with different particle radii and C-rates: (a) 5 μm, 1 C-rate; (b) 5 μm, 5 C-rate; (c) 10 μm, 1 C-rate; (d) 10 μm, 5 C-rate.

to 10 μm, an entire separation also occurs at 1 C-rate. However, no debonding is observed at 5 C-rate.

These results show that interface debonding is more likely to happen at a smaller particle size and a lower C-rate. This trend is opposite to the fracture behavior inside a particle, where fracture is more likely to happen at a larger particle size and a higher C-rate. Table 3 summarizes the maximum principal stress at the edge of the binder. It is clearly observed that the stress level at the interface decreases as the C-rate and particle size increases. We attribute the distinct fracture behaviors at the particle/binder interface and inside a particle to different mechanisms of stress generation. For interface debonding, the stress at the interface mainly comes from the expansion of the particle during lithium intercalation relative to the binder. As the C-rate decreases, it takes longer time for the concentration on the particle surface to reach stoichiometry or a certain SOC. Thus there is enough time for lithium ions to diffuse deeply inside the particle, and the concentration inside the particle is more uniform. As a result, the total amount of lithium ions intercalated is larger at a lower C-rate, leading to a larger volume expansion and strain at the interface. As the particle size increases, more space is available for lithium ions to fill, which leads to a smaller volume expansion. Therefore, a larger volume expansion at a low C-rate with a smaller particle size causes a larger stress at the interface, which leads to interface fracture more likely to occur.

In contrast, the mechanical stress inside a particle is related to the gradient of lithium concentration. Fig. 6 compares two cases in terms of the stress field and the corresponding lithium concentration profile at a fully charged state. For the case of 10 μm and 5 C-rate, the lithium concentration gradient is larger than the case of 5 μm and 1 C-rate. The larger concentration gradient causes a larger stress inside the particle, which reaches almost 90 MPa. On the other hand, for the case of 5 μm and 1 C-rate, it shows a relatively uniform distribution of lithium ions and the stress within the particle is less than 50 MPa.

Table 3
The maximum principal stress at the edge of the binder at 100% SOC.

Particle radius (μm)	1 C (MPa)	5 C (MPa)
5	205	170
10	184	60

It is worth mentioning that geometries such as the contact angle between the binder and particle may affect the stress level. However, our study focuses on how the stress associated with electrochemical responses affect fracture at the interface during battery operation. Our main conclusion is that the interface fracture is caused by the volume change of the particle. For this purpose, the spherical particle is sufficient as a representative structure for our conclusion.

4. Conclusion

Debonding at the particle/binder interface was simulated using an integrated electrochemical–mechanical model and cohesive zone model. The simulations show that fracture at the interface occurs more likely at a smaller particle size and a lower C-rate, which is opposite to the tendency of fracture inside a particle. The reason is that the interface debonding is caused by the overall expansion of the particle, while fracture inside a particle is caused by the concentration gradient. The simulations show that

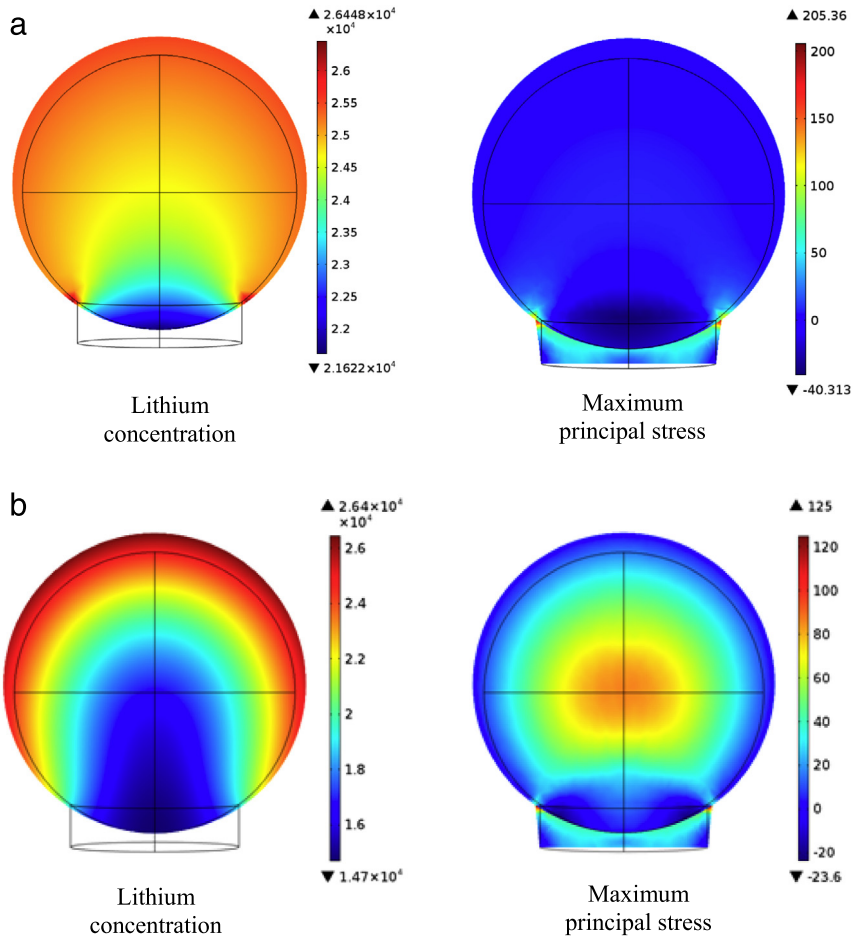

Fig. 6. Comparison of the lithium concentration profile (left) and stress field (right). (a) 5 μm and 1 C-rate and (b) 10 μm and 5 C-rate.

debonding begins to occur at 85% SOC with a particle radius of 5 μm and 1 C-rate, which indicates that controlling the SOC window can help to avoid debonding at the particle/binder interface. In addition, the cohesive zone model enables measuring the actual area of the new interface created by fracture. The framework can be used to predict the increase of exposed surfaces to electrolyte due to crack in the particle network, which can be linked to further side reactions and SEI formation.

Acknowledgments

This research was funded by the GM/UM Advanced Battery Coalition for Drivetrains and the UM-SJTU collaborative research grant. Support from our sponsors is gratefully acknowledged.

References

[1] R.A. Huggins, W.D. Nix, Decrepitation model for capacity loss during cycling of alloys in rechargeable electrochemical systems, Ionics 6 (2000) 57–63.
[2] D. Wang, X. Wu, Z. Wang, L. Chen, Cracking causing cyclic instability of $LiFePO_4$ cathode material, J. Power Sources 140 (2005) 125–128.
[3] H.-L. Zhang, F. Li, C. Liu, J. Tan, H.-M. Cheng, New insight into the solid electrolyte interphase with use of a focused ion beam, J. Phys. Chem. B 109 (2005) 22205–22211.
[4] K. Zhao, M. Pharr, J.J. Vlassak, Z. Suo, Fracture of electrodes in lithium-ion batteries caused by fast charging, J. Appl. Phys. 108 (2010) 073517.
[5] W.H. Woodford, Y.-M. Chiang, W.C. Carter, Electrochemical shock of intercalation electrodes: A fracture mechanics analysis, J. Electrochem. Soc. 157 (2010) A1052–A1059.
[6] T.K. Bhandakkar, H. Gao, Cohesive modeling of crack nucleation in a cylindrical electrode under axisymmetric diffusion induced stresses, Internat. J. Solids Struct. 48 (2011) 2304–2309.
[7] M. Zhu, J. Park, A.M. Sastry, Fracture analysis of the cathode in Li-ion batteries: A simulation study, J. Electrochem. Soc. 159 (2012) A492–A498.
[8] R. Grantab, V.B. Shenoy, Location- and orientation-dependent progressive crack propagation in cylindrical graphite electrode particles, J. Electrochem. Soc. 158 (2011) A948–A954.
[9] R. Grantab, V.B. Shenoy, Pressure-gradient dependent diffusion and crack propagation in lithiated silicon nanowires, J. Electrochem. Soc. 159 (2012) A584–A591.
[10] S. Lee, J. Park, J. Yang, W. Lu, Molecular dynamics simulations for traction–separation responses at the interface of PVDF binder and graphite materials in the electrode of Li-ion batteries, J. Electrochem. Soc. 161 (2014) A1218–A1223.
[11] J. Park, W. Lu, A.M. Sastry, Numerical simulation of stress evolution in lithium manganese dioxide particles due to coupled phase transition and intercalation, J. Electrochem. Soc. 158 (2011) A201–A206.
[12] X. Zhang, W. Shyy, A. Marie Sastry, Numerical simulation of intercalation-induced stress in Li-ion battery electrode particles, J. Electrochem. Soc. 154 (2007) A910–A916.
[13] S. Li, M.D. Thouless, A.M. Waas, J.A. Schroeder, P.D. Zavattieri, Use of mode-I cohesive-zone models to describe the fracture of an adhesively-bonded polymer-matrix composite, Compos. Sci. Technol. 65 (2005) 281–293.

[14] N. Chandra, H. Li, C. Shet, H. Ghonem, Some issues in the application of cohesive zone models for metal–ceramic interfaces, Internat. J. Solids Struct. 39 (2002) 2827–2855.
[15] W. Li, T. Siegmund, An analysis of crack growth in thin-sheet metal via a cohesive zone model, Eng. Fract. Mech. 69 (2002) 2073–2093.
[16] S. Song, G. Paulino, W. Buttlar, Simulation of crack propagation in asphalt concrete using an intrinsic cohesive zone model, J. Eng. Mech. 132 (2006) 1215–1223.
[17] B.R.K. Blackman, H. Hadavinia, A.J. Kinloch, J.G. Williams, The use of a cohesive zone model to study the fracture of fibre composites and adhesively-bonded joints, Int. J. Fract. 119 (2003) 25–46.
[18] Y.F. Gao, A.F. Bower, A simple technique for avoiding convergence problems in finite element simulations of crack nucleation and growth on cohesive interfaces, Modelling Simul. Mater. Sci. Eng. 12 (2004) 453–463.
[19] S.M. Xia, Y.F. Gao, A.F. Bower, L.C. Lev, Y.T. Cheng, Delamination mechanism maps for a strong elastic coating on an elastic–plastic substrate subjected to contact loading, Internat. J. Solids Struct. 44 (2007) 3685–3699.
[20] Y. Qi, S.J. Harris, In situ observation of strains during lithiation of a graphite electrode, J. Electrochem. Soc. 157 (2010) A741–A747.
[21] Q. Chen, D. Natale, B. Neese, K. Ren, M. Lin, Q.M. Zhang, M. Pattom, K.W. Wang, H. Fang, E. Im, Piezoelectric polymers actuators for precise shape control of large scale space antennas, Electroact. Polym. Actuators Dev. 6524 (2007) 65241.
[22] V.A. Sethuraman, A. Nguyen, M.J. Chon, S.P.V. Nadimpalli, H. Wang, D.P. Abraham, A.F. Bower, V.B. Shenoy, P.R. Guduru, Stress evolution in composite silicon electrodes during lithiation/delithiation, J. Electrochem. Soc. 160 (2013) A739–A746.
[23] J. Pu, X. Yan, Y. Jiang, C. Chang, L. Lin, Piezoelectric actuation of direct-write electrospun fibers, Sensors Actuators A 164 (2010) 131–136.
[24] C. Byrappa, B.S. Ajay Kumar, M.V. Chandrashekar, A.S. Karthikeyan, Finite element analysis of PVDF actuated cantilever beams, Int. J. Innov. Res. Dev. 2 (2013) 239–245.
[25] X. Lin, J. Park, L. Liu, Y. Lee, A.M. Sastry, W. Lu, A comprehensive capacity fade model and analysis for Li-ion batteries, J. Electrochem. Soc. 160 (2013) A1701–A1710.
[26] J. Christensen, J. Newman, Stress generation and fracture in lithium insertion materials, J. Solid State Electrochem. 10 (2006) 293–319.